EPJ Photovoltaics **11**, 2 (2020)

https://doi.org/10.1051/epjpv/2019011

Available online at:
www.epj-pv.org

REGULAR ARTICLE OPEN ACCESS

Nanomolded buried light-scattering (BLiS) back-reflectors using dielectric nanoparticles for light harvesting in thin-film silicon solar cells

Derese Desta[1], Rita Rizzoli[2], Caterina Summonte[2], Rui N. Pereira[1], Arne Nylandsted Larsen[3], Peter Balling[3], and Sanjay K. Ram[3,4,*]

[1] Department of Physics and I3N, University of Aveiro, Campus Universitário de Santiago, 3810-193 Aveiro, Portugal
[2] IMM-Consiglio Nazionale delle Ricerche, via Gobetti 101, 40129 Bologna, Italy
[3] Department of Physics and Astronomy – iNANO, Aarhus University, Gustav Wieds Vej 14, 8000 Aarhus C, Denmark
[4] Department of Physics, Amrita School of Arts and Sciences, Amrita Vishwa Vidyapeetham, Kollam 690525, Kerala, India

Received: 1 October 2019 / Received in final form: 19 November 2019 / Accepted: 17 December 2019

Abstract. The article presents a nanoparticle-based buried light-scattering (BLiS) back-reflector design realized through a simplified nanofabrication technique for the purpose of light-management in solar cells. The BLiS structure consists of a flat silver back-reflector with an overlying light-scattering bilayer which is made of a TiO_2 dielectric nanoparticles layer with micron-sized inverted pyramidal cavities, buried under a flat-topped silicon nanoparticles layer. The optical properties of this BLiS back-reflector show high broadband and wide angular distribution of diffuse light-scattering. The efficient light-scattering by the buried inverted pyramid back-reflector is shown to effectively improve the short-circuit-current density and efficiency of the overlying n-i-p amorphous silicon solar cells up to 14% and 17.5%, respectively, compared to the reference flat solar cells. A layer of TiO_2 nanoparticles with exposed inverted pyramid microstructures shows equivalent light scattering but poor fill factors in the solar cells, indicating that the overlying smooth growth interface in the BLiS back-reflector helps to maintain a good fill factor. The study demonstrates the advantage of spatial separation of the light-trapping and the semiconductor growth layers in the photovoltaic back-reflector without sacrificing the optical benefit.

Keywords: inverted pyramids / light management / photovoltaics / thin-film solar cells / nanoparticles / nanomolding

1 Introduction

The advantages of silicon thin-film solar cells such as the low consumption of raw material and the possibility of large-area fabrication, are counterbalanced by the reduced absorption of incident light in the thin absorber layer [1,2]. As we aim for thinner solar cells, light-trapping strategies become crucial to compensate for the loss in photovoltaic energy-conversion efficiency arising from photon losses [3–5]. Textured interfaces and surfaces have been exploited in silicon solar cells for nanophotonic and plasmonic light-trapping [6–8]. However, the success of an effective photon harvesting scheme based on any configuration of optical structures finally hinges on the performance of the solar cell fabricated on those structures, and often a trade-off is involved in balancing the two aspects.

Among various kinds of structures explored for their light-trapping performance, upright pyramidal and inverted pyramidal nano- and microstructures are extensively studied in crystalline silicon solar cells [9–11], but less so in the context of silicon thin-film solar cells [12,13]. In these studies, on crystalline silicon solar cells, various experimental and modeling studies have brought out the different beneficial anti-reflection effects of the pyramidal and the inverted pyramidal structures on the top surface [14,15]. Some studies have shown front side periodic inverted pyramid structures to outperform pyramidal structures in enhancing light absorption in crystalline silicon solar cells [14]. Nanoscale inverted pyramids with suitable configuration on a silicon wafer were shown to be useful in light trapping in ultra-thin c-Si solar cells [16] and a n-i-p amorphous silicon (a-Si:H) single junction solar cell [13]. Nevertheless, it is difficult to incorporate inverted pyramidal micron-scaled structures (or structures like pillars or pyramids) [15,17,18] into back-reflectors without

* e-mail: sanjayk.ram@gmail.com

adversely affecting the growth of conformal semiconductor thin film layers and thus leading to deterioration of the solar cell properties [12,19–24].

Apart from manipulation of light using different configurations of nano- or microstructures, recently, some studies have theorized the benefit of exploiting the refractive indices of materials to manipulate light to enhance the optical absorption in solar cells [7,8,25,26]. Dielectric nanoparticles, due to their unique optical and structural properties, are emerging as highly manipulable building blocks to fabricate nano- and microstructures [27–29]. We have previously demonstrated a light-trapping nano-crater back-reflector fabricated by molding of TiO_2 nanoparticles (TiO_2-NP) [30], and recently we presented, a buried light-scattering (BLiS) back-reflector using TiO_2-NPs molded into pyramidal microstructures buried within a flat top layer of silicon nanoparticles (Si-NP) [23]. TiO_2 nanoparticles are transparent with a low refractive index while Si-NPs have a higher refractive index and are optically similar to the a-Si:H material of the solar cell that is fabricated on the back-reflector.

Applying theoretically promising optical designs of back-reflectors in solar cell devices throws up the challenge of extensive optimization of growth conditions to reconcile solar cell quality with substrate roughness. This feasibility problem, while possibly surmountable in the laboratory setting, may prove to be prohibitive for scaling up the design to industrial manufacturing. The BLiS structures that we demonstrate mitigates the detrimental effect of the morphological roughness created by texturing, namely, the formation of cracks and porous areas in the silicon layers with a deterioration of solar-cell efficiency and stability. Further, the BLiS approach does not require processing steps using lithography and etching that can lead to scalability issues [31,32].

In this work, we use the BLiS approach to apply micron-sized light-manipulating structures that are usually considered incompatible with good electrical performance, for light harvesting in thin-film solar cells. A simplified nanofabrication technique utilizing nanoparticles is employed to create a light-management bi-layer consisting of a TiO_2-NP layer containing inverted pyramidal-shaped microcavities, which are filled with Si-NPs with the interfacial top surface of the Si-NP layer being flat. The design architecture of this arrangement is schematically drawn in Figure 1.

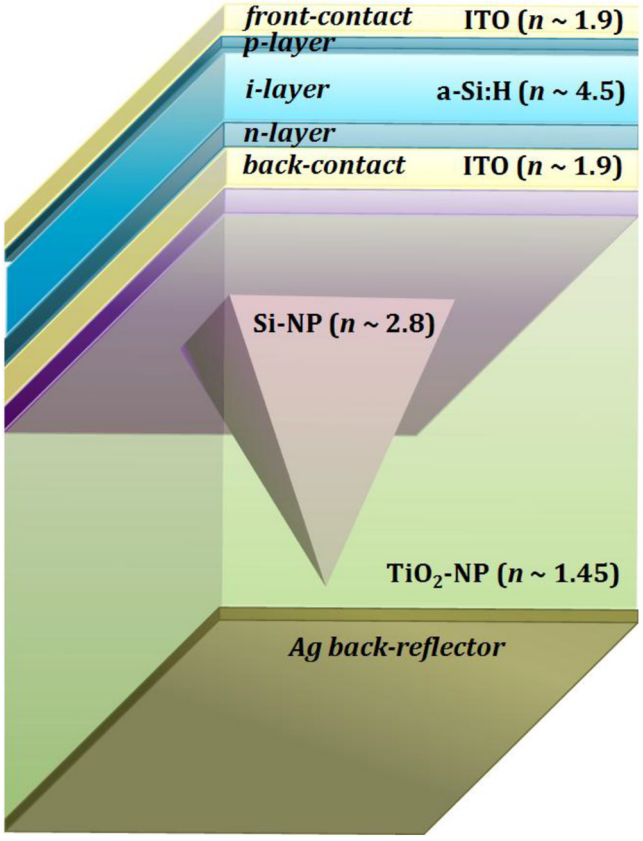

Fig. 1. Schematic illustration of BLiS back-reflector for n-i-p Si thin film solar cells. The TiO_2-NP layer over the planar silver back-reflector has inverted pyramidal shaped microcavities, which is further covered by a flat-topped Si-NP layer.

2 Experimental and modeling details

Three types of substrates were used for the studies consisting of three different types of back-reflectors: planar, inverted pyramids and buried inverted pyramids. For the planar back-reflector, pre-cleaned and baked glass substrates were coated with Ti, Ag and Al-doped zinc oxide (AZO) to create the Glass/Ti(10 nm)/Ag (120 nm)/AZO(30 nm) back-reflector stack. The metal layers were deposited using an electron-beam evaporation technique and AZO was sputtered using an AJA ATC Orion rf-magnetron system. The substrate with the planar back-reflector is denoted as the flat surfaced back-reflector (Flat-BR), on which the reference solar cell was deposited.

To create the inverted pyramid back-reflector (IP-BR) and buried inverted pyramid back-reflector (BIP-BR) substrates, planar back-reflector substrates were further coated with a thin (100 nm) TiO_2 layer by rf-magnetron sputtering to avoid the oxidation of Ag in the subsequent sintering steps. The anatase TiO_2-NP were purchased from Sigma Aldrich and have an average size of 20 nm.[1] TiO_2-NP paste was spin-coated on these substrates and then molded with a pyramid-textured PDMS stamp, to create randomly distributed hollow-core inverted pyramidal structures made of TiO_2-NPs on the planar reflector, designated as the IP-BR.

To bury the pyramidal structures of the IP-BR, Si-NP paste was spin-coated on top of the TiO_2-NP textured surfaces and leveled out by pressing it with a flat PDMS stamp leading to a BLiS architecture. These Si-NPs having a mean diameter of 4.9 nm, were synthesized by microwave-assisted decomposition of silane [33,34]. The details of the nanomolding process used can be found in our previously reported work [23]. The Si-NP coating step results in the BIP-BR which has a random distribution of TiO_2-NP inverted pyramids buried within the Si-NPs

[1] www.sigmaaldrich.com

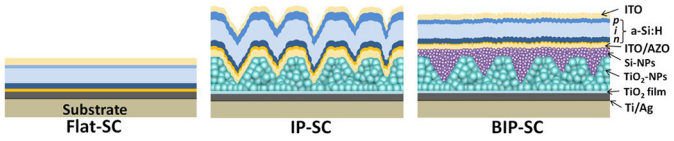

Fig. 2. The cross-sectional schematic illustrations of the n-i-p a-Si:H solar cells grown on Flat-BR (Flat-SC), IP-BR (IP-SC) and BIP-BR (BIP-SC).

bilayer, on the original planar reflector. To provide back contact to the solar cells, 100 nm thick indium tin oxide (ITO) and 30 nm aluminum zinc oxide (AZO) were sputtered on top of the nanoparticle layer surface [30].

The n-i-p type a-Si:H thin-film solar cells were fabricated on these reflectors in a cluster type PECVD system in a single run to ensure identical deposition condition. The doped and undoped a-Si:H thin films were deposited in separate chambers of the reactor. The thickness of the a-Si:H absorber layer was kept low at ~250 nm to avoid light-induced degradation [4]. The thicknesses of the p-doped and n-doped a-Si:H layers were 10 and 30 nm, respectively. Finally, a 70 nm thick ITO layer was deposited on each solar cell using shadow masking in the rf-magnetron sputtering system to provide the front contact to the device. The cross-sectional schematic illustrations of the n-i-p a-Si:H solar cells grown on the Flat-BR (Flat-SC), the IP-BR (IP-SC) and the BIP-BR (BIP-SC) are shown in Figure 2.

The surface topography of the solar cells was studied using atomic force microscopy (AFM, Bruker Dimension Edge) and the cross-sectional analysis of the solar cell devices was carried out using a focused ion beam instrument (FIB, FEI VERSA 3D). The optical properties of the back-reflectors and solar cell devices were studied using a spectrometer equipped with a 150 mm integrating sphere (Perkin Elmer Lambda 1050). The solar cell current density vs. voltage (J–V) characteristics under one sun illumination were measured at 100 mW/cm^2 AM1.5 irradiance using a calibrated Oriel solar simulator with a xenon arc lamp. The external quantum efficiency (EQE) measurements were carried out using a setup calibrated with a reference cell, including a stable white light lamp, interference filters, a bias light, a chopper, and a lock-in amplifier.

The numerical absorption profile calculation was performed using finite-difference time-domain (FDTD) simulation software from Lumerical.[2] The details of the FDTD modeling are presented in the supplementary section (Fig. S1) and in previously reported work [23,30]. Briefly, the physical model of the solar cell structure was based on imported topographical data obtained from AFM images of back-reflectors and the layer thicknesses obtained from cross-sectional FIB-SEM images of the solar cells, as shown in Figure S2. The optical parameters (like spectral variation of refractive indices and dielectric constants) of the constituent layers of the solar cells (except Ag [35]) were obtained from spectroscopic ellipsometry studies of the individual layers.

3 Results and discussion

The IP-BR surface shows a root-mean-square roughness (σ_{rms}) value of ~548 nm and consists of randomly placed inverted pyramidal features (with lateral feature sizes in the range of 1–5 μm) with square bases. In contrast, the BIP-BR surface reveals an almost flat surface with σ_{rms} value of ~18.5 nm, with the Si-NPs having filled up the cores of the TiO_2-NP inverted pyramids. The top surface of the BIP-BR in the cross-sectional view shows shallow and very broad (>15 μm) waves implying that despite the absolute roughness value of ~18.5 nm, the surface morphology does not consist of densely spaced or sharp peaks. The morphological images of the top surfaces of the IP-BR and BIP-BR structures obtained by AFM and the SEM image of the FIB milled cross-section of an a-Si:H solar cell deposited on BIP-BR are shown in Supplementary Figure S2.

To further ascertain how smooth the surface really is, especially in the presence of a random distribution of features in the back-reflector, we turn to the autocorrelation function, which expresses how the surface is correlated to itself at a certain distance.[3] The deduced autocorrelation lengths for the BIP-BR and the IP-BR surfaces are 3.53 μm and 1.97 μm, respectively. Considering the σ_{rms} values, the autocorrelation length substantiates the conclusion that burying the inverted pyramid layer of TiO_2-NP and filling in the hollow inverted pyramids with Si-NP makes the top surface of the BIP-BR smooth. The smoothness of the substrate surface is crucial for the growth of good quality solar cells and is one of the main objectives of this work.

To investigate the light-scattering properties of the IP-BR, the BIP-BR, and the F-BR, we carried out reflection measurements over a broad optical range (from UV-visible 300 nm to IR 2000 nm) using an integrating sphere. The total reflection (R_T) and diffuse reflection (R_D) of the IP-BR, the BIP-BR and the F-BR structures are shown in Figure 3a. The excellent reflecting property of the inverted pyramidal structures, almost like that of Flat-BR, is indicated by their high total reflectance values. Some absorption detected in the 400–600 nm wavelength range of the light is associated with the absorption in the TiO_2-NP and in the TiO_2 thin film underneath. In the case of the BIP-BR, we observe reflecting properties very similar to the IP-BR, apart from an additional, albeit small, loss in the total reflectance for $\lambda < 600$ nm. This can be ascribed to the absorption of light in the Si-NP layer, since in the BIP-BR structure, besides the TiO_2-NP with the onset of absorption at about 320 nm, also present are the Si-NPs, which have an onset of absorption at ~500 nm. Moreover, in the light trapping region of the a-Si:H solar cell (600–800 nm), both IP-BR and BIP-BR show very high total reflectance values that are close to that of the F-BR. The

[2] Lumerical Solutions, Inc., http://www.lumerical.com/tcad-products/fdtd/

[3] http://gwyddion.net/documentation/user-guide-en/statistical-analysis.html

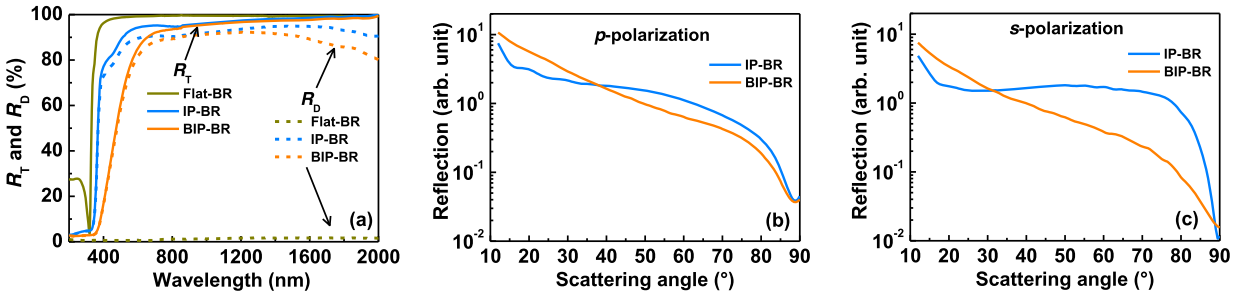

Fig. 3. Total reflectance (R_T, solid lines) and diffuse reflectance (R_D, dashed lines) of Flat-BR, IP-BR, and BIP-BR (a), and angle-resolved scattering measurements of IP-BR and BIP-BR (b and c).

loss in reflectance due to the absorption in the wavelength range of $400 < \lambda < 600$ nm in both IP-BR and BIP-BR, however, is not detrimental, since the incident light in this spectral range is completely absorbed by the active layer of the n-i-p solar cell before reaching the back-reflector.

The very high diffuse-reflectance values (>90% of total reflectance) of the IP-BR over a broad optical range can be understood as the consequence of multiple reflections of light occurring at the oblique interfaces of the inverted pyramidal structures. In addition, omnidirectional scattering of light also takes place at the nanotextured surfaces, arising from the component nanoparticles and within the optically inhomogeneous structures comprising of voids, and variably sized nanoparticles and their clumps. Interestingly, similar high diffuse-reflectance values are observed for the BIP-BR structure over the same optical range as in the case of the IP-BR, which can be attributed to the multiple light reflections and the abundant light-scattering taking place at the buried textured interfaces.

In order to evaluate the angular distribution of the reflected light from the IP-BR and the BIP-BR, a red laser beam ($\lambda = 633$ nm) was used at normal incidence to the sample, and the reflection intensity distributions for both *s*- and *p*-polarization as a function of the scattering angle were recorded. The angular distribution of the diffusely reflected light from the IP-BR and the BIP-BR is shown in Figure 3b and c, respectively, for *p*- and *s*-polarized light ($\lambda = 633$ nm) incident normal to the surface. For both *s*- and *p*-polarizations, the IP-BR and BIP-BR exhibit scattering over a broad angular range with a significant part of scattering occurring at large oblique angles, which can be expected to result in efficient photon harvesting in a solar cell.

It is to be noted that the optical properties of the BIP-BR are not degraded compared to the IP-BR, despite burying the inverted pyramid layer with another layer of Si-NP with a resulting flat top surface. The optical properties of the nanoparticles are also important to understand how the nanoparticle microstructures manipulate light in the back reflector. The unabsorbed incident light with wavelength above roughly 500 nm that penetrates into the layers of the back-reflector progressively enters materials/zones of lower refractive indices (refractive indices deduced for Si-NPs and TiO_2-NPs are ~2.8 and ~1.45, respectively, at $\lambda = 500$ nm) [23] leading to an oblique path of the light when it hits the Ag reflecting surface, resulting in more scattering and a longer path length of the reflected photon. The 4.9 nm average diameter Si-NPs used in this study have a larger bandgap (~1.6 eV due to quantum confinement) and scatter the light without much absorption. Higher bandgap small-sized Si-NP would lead to even less parasitic losses but a poorer scattering of light due to the lower refractive index.

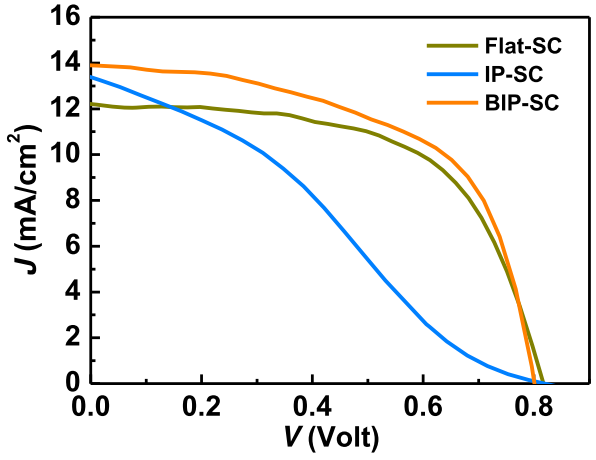

Fig. 4. *J*–*V* characteristics of n-i-p a-Si:H thin-film solar cells made on Flat-BR, IP-BR, and BIP-BR.

The current–voltage (*J*–*V*) characteristics of the n-i-p solar cells fabricated on the F-BR, the IP-BR, and the BIP-BR are shown in Figure 4. The average device performance parameters of five typical solar cells from each device are mentioned in Table 1. The efficiency (η) of the solar cell on F-BR is 5.87% with a short circuit current density (J_{sc}) of ~12.2 mA/cm^2 and a fill factor (FF) of ~59%. The performance of the a-Si:H made directly on IP-BR is seen to be deteriorated, yielding FF and η values of 30% and 3.31%, respectively, despite showing improvement in the J_{sc} (13.4 mA/cm^2). On the other hand, the J_{sc}, FF and η values of the BIP-SC are 13.9 mA/cm^2, 62%, and 6.9%, respectively. The efficiency of the BIP-SC is nearly 17.5% higher than that of the Flat-SC. The reason for such a large improvement in BIP-SC device performance is due to the ~9.8% improvement in its J_{sc} compared to the Flat-SC because the open-circuit voltage and the FF values are nearly comparable in the two devices.

Table 1. Summary of performance characteristics for the n-i-p a-Si:H solar cells fabricated on flat, inverted pyramids, and buried inverted pyramid back-reflector surfaces. The enhancements in J_{sc} and η are calculated using $\Delta J_{sc} = [(J_{sc\text{-}IP(BIP)\text{-}SC} - J_{sc\text{-}Flat\text{-}SC})/J_{sc\text{-}Flat\text{-}SC}] \times 100$ % and $\Delta\eta = [(\eta_{IP(BIP)\text{-}SC} - \eta_{Flat\text{-}SC})/\eta_{Flat\text{-}SC}] \times 100\%$ respectively.

Device	V_{oc} (mV)	FF (%)	η (%)	$\Delta\eta$ (%)	J_{sc} (mA cm^2)	ΔJ_{sc} (%)	$J_{sc\text{-}FDTD}$ (mA cm^2)	$\Delta J_{sc\text{-}FDTD}$ (%)
Flat-SC	815 ± 1	59.0 ± 0.5	5.87	–	12.2 ± 0.1	–	12.3	–
IP-SC	818 ± 1	30.2 ± 0.1	3.31	–43.6	13.4 ± 0.1	9.8		
BIP-SC	801 ± 1	62.0 ± 0.2	6.90	17.5	13.9 ± 0.2	13.9	14.5	17.9

The distribution of growing layers over the large textures over an increased surface area in the IP-BR is expected to lead to non-conformal film growth and sub-optimal film thickness. Combined with the fact that the doped and intrinsic buffer layers are very thin, the non-conformal film growth may lead to discontinuities in the layer conforming to the rough top surface of the IP-BR. An indirect indication of this is seen in the form of the distortion in the J–V curve of the IP-SC device, where the inflection point close to the V_{oc} creates an S-shaped behavior, highlighting a distinct difference between the performances of the IP-SC and the BIP-SC. This S-shape of the J– V curve is a sign of non-optimal carrier collection in the device that results from the defects in the solar cell layers [36–38]. Many different solar cell designs based on nanomaterials and nanotextures have been reported that decouple light absorption and carrier extraction leading to increased efficiency [39]. In the case of the IP-SC and other such rough textures, the intended optical benefit is obtained due to the increased scattering induced by the textures, but it is often at the cost of the electrical performance due to shunts and defects associated with the rough interfaces of the solar cell layers. In BIP-SC, we are able to address these electrical issues by keeping the benefit of the increased photon path length while creating smooth interfaces of the electrically active solar-cell layers. The textures and interfaces of the NPs layers influence the optical properties by affecting the photon paths in the solar cell but are isolated from the charge-carrier paths.

Next, we investigate how much of the improvement in the performance of the BIP-SC can be attributed to the light-scattering properties of the BIP-BR. To understand the light-trapping effect, we measure the total optical absorption (1-R_T) of the a-Si:H solar cells deposited on top of the F-BR and the BIP-BR, as shown in Figure 5a. It can be seen from Figure 5a that the Flat-SC and the BIP-SC devices have comparable absorption in the short-wavelength region (<600 nm). On the other hand, the absorption of the BIP-SC shows significant improvement at long wavelengths (>600 nm) when compared to the Flat-SC device. This clearly demonstrates that the enhancement in absorption in the long wavelength region is due to efficient light trapping by the BIP-BR.

The wavelength-dependent external quantum efficiency (EQE) and the corresponding EQE ratio ($EQE_{BIP\text{-}SC}/EQE_{F\text{-}SC}$) of the Flat-SC and the BIP-SC devices shown in Figure 5b further indicate that the improvement in the performance of the BIP-SC device is due to the enhanced trapping of long wavelength light. Figure 5b clearly depicts

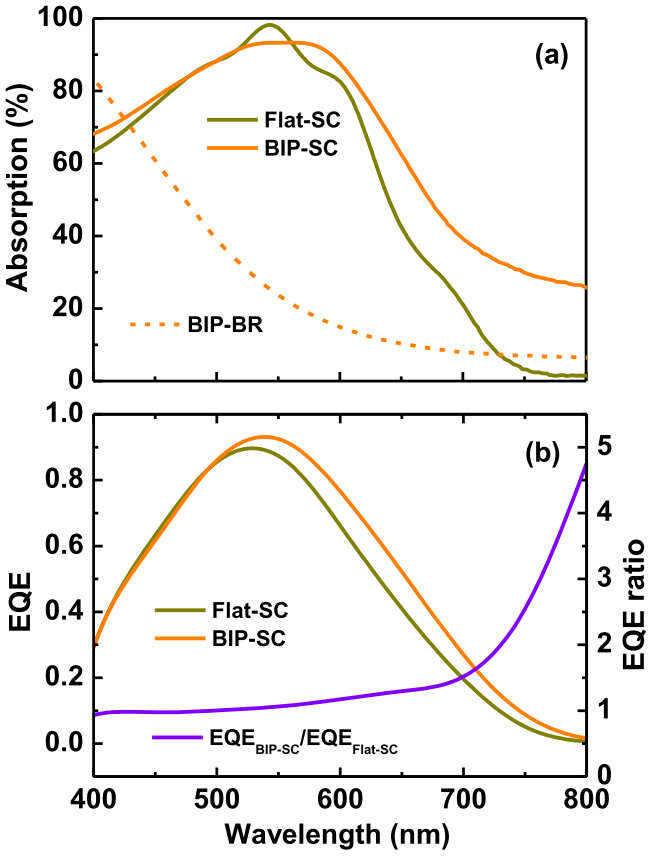

Fig. 5. (a) Total optical absorption by Flat-SC and BIP-SC devices (solid lines), and parasitic absorption by the BIP-BR (dashed line); (b) measured EQE (left-hand side y-axis) spectra of Flat-SC and BIP-SC devices and EQE ratio (right-hand side y-axis).

the spectral region where the BIP-SC device outperforms the Flat-SC device. The EQE of the BIP-SC starts rising in the wavelength region above 600 nm due to the efficient scattering of the incident light by the BIP-BR in this region, with a very significant rise in long wavelength region $\lambda > 700$ nm.

An optical modeling study of the solar cells (Flat-SC and BIP-SC) is important to improve and validate our understanding of the mechanisms responsible for the enhanced light-absorption and solar cell efficiency. Figure S3 compares the simulated and measured light-absorption spectra of the Flat-SC and the BIP-SC devices. The absorption spectra of these devices were simulated considering the entire depth of the device using

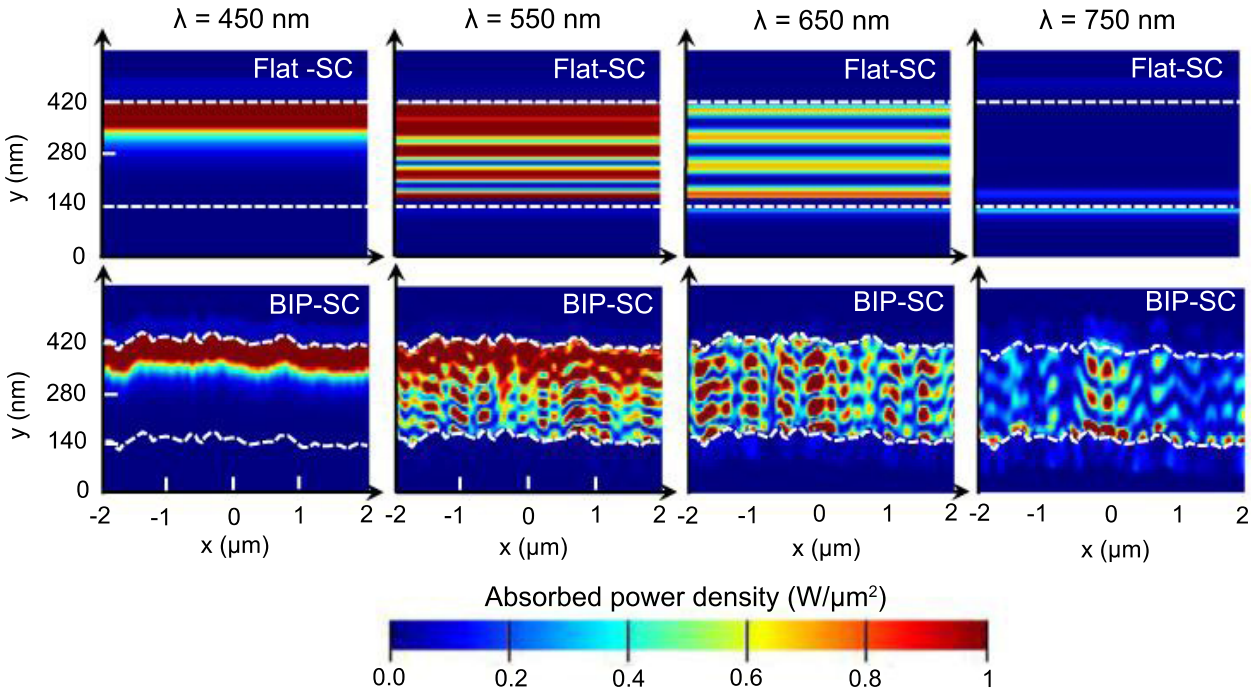

Fig. 6. The calculated optical absorption distribution at wavelength values of 450 nm, 550 nm, 650 nm and 750 nm for a-Si:H thin-film solar cells (Flat-SC and BIP-SC). The dotted lines are added to demarcate the a-Si:H thin-film.

the optical model shown in supplementary Figure S1 comprising various layers, including the nanoparticle layers in the case of BIP-SC. Despite the non-idealities in the simulation parameters, good agreement is obtained between the experimentally measured and the simulated absorption curves for the solar cells. However, in the case of BIP-SC, the simulated absorption profile displays some peaks at long wavelength region, which originate from the interference of light within the thick TiO_2-NP/Si-NP stack because of the use of periodic and perfectly matched layer boundary conditions (Fig. S1).

Figure 6 presents the simulated spatial distribution of optical absorption in the constituent layers of the Flat and BIP solar cells at light wavelengths of 450 nm, 550 nm, 650 nm, and 750 nm. The quantitative estimation of the absorbed power density (in $W/\mu m^2$) can be deduced from the color scale shown in the figure. The top layer of the a-Si:H solar cell completely absorbs the short wavelength light ($\lambda = 450$ nm). Fabry-Perot type resonances within the film are more prominent in the Flat-SC at longer wavelengths (>550 nm), while the BIP-SC shows the propagation of trapped light within the solar cell. The Flat-SC shows an overall low absorption at 650 nm, with most of the absorption confined to the n-doped region of the solar cell. On the other hand, diffuse high absorption spots throughout the a-Si:H absorber layer are visible in the absorption profile of the BIP-SC. In the case of the 750 nm wavelength light, a substantial amount of absorption is still taking place in the BIP-SC, while the absorption in the Flat-SC has dropped to negligible values, which correlates well with the results obtained from the experimental and theoretical studies. The visual representation of the calculated optical absorption distribution of the devices presented in Figure 6 includes the absorption profiles of the devices till ~140 nm beneath the solar cell layer (below the broken line), which is the region of Si-NPs in BIP-SC. The absorption distribution in the small portion of the Si-NPs layer shown in the images for BIP-SC clearly indicates negligible absorption (dark blue in the color scale) for the short wavelength region ($\lambda < 650$ nm) and very low even for the long wavelengths ($\lambda > 650$ nm) (dark blue with small light blue patches in the color scale). The short-circuit-current density was calculated using equation (S-4) described in the Supplementary section/document, considering only the optical absorption taking place in the *i*-layer of the solar cells. The calculated J_{sc} values for the BIP-SC and the Flat-SC are 14.5 mA/cm^2 and 12.3 mA/cm^2, respectively, as presented in Table 1. These calculated J_{sc} values are close to the experimentally measured values, especially in the Flat-SC, thus validating our model.

We have so far established that the light trapping effect of the optical surfaces of the buried TiO_2 microstructures within the Si-NP layer results in an enhancement of the solar cell performance. However, another cause of light trapping may be the surface roughness of the Si-NP layer on which the solar cell is grown, making it important to explore whether the surface features of the Si-NP layer also lead to improved absorption of the incident light. The surface roughness σ_{rms} of the as-prepared BIP-BR is 18.7 nm, which after the complete solar cell deposition process, can be expected to lead to a slightly lower roughness of the top surface of the silicon layer. Any contribution to light-trapping from the Si-NP layer with σ_{rms} ~18.7 nm should lead to a higher EQE in the spectral range below 500 nm, which is notably absent in Figure 4b. This, along with the very large autocorrelation length

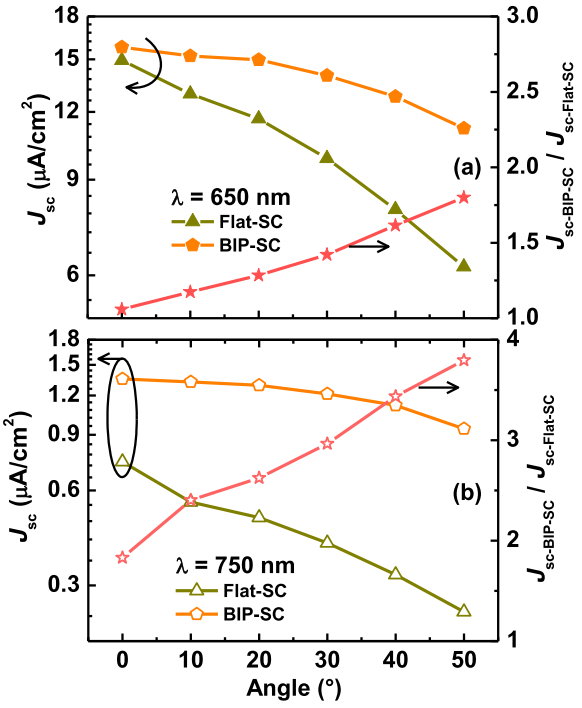

Fig. 7. The J_{sc} angular dependence of the BIP-SC and the Flat-SC devices for two wavelengths of unpolarized light, 650 nm and 750 nm, is shown in the left y-axes of the (a) and (b) parts respectively. The right y-axes of these graphs show the angular dependence of the J_{sc} ratio (J_{sc}-BIP-SC/J_{sc}-Flat-SC) for these two wavelengths of light.

~3.5 μm, negates the possibility of enhancement in the photocurrent in the BIP-SC being due to any anti-reflection or light-trapping improvements arising from the surface morphology of the Si-NP layer [40,41]. Rather, it is decidedly the light trapping effectuated by the optical interfaces within the BLiS back reflector that leads to the enhancement in the photocurrent in the solar cell on it.

An important aspect of any light-harvesting approach is the effect of the variability of the incidence angle of sunlight on the light collection. With normal incident light, good gain in photocurrent and efficiency was obtained in the BIP-SC compared to the Flat-SC. A broad angular range of scattering of light by the IP-BR and the BIP-BR was seen in Figure 3, which should translate into a better solar cell performance over a broad angular range as well. The J–V characteristics of the Flat-SC and BIP-SC were measured for different angles of incidence for light of wavelengths 650 nm and 750 nm. The long wavelengths of light, which are less absorbed by a-Si:H material, are useful for gathering information about the light scattering occurring specifically at the back of the cell. The angular dependencies of J_{sc} for the BIP-SC and the Flat-SC devices are shown on the left y-axes of Figure 7a and b, while the right y-axes show the angular dependence of the J_{sc} ratio ($J_{sc\text{-BIP-SC}}/J_{sc\text{-Flat-SC}}$) for the two wavelengths. The drop in the J_{sc} of the BIP-SC is less steep than seen with the J_{sc} of the Flat-SC device. At 40° angle of incidence, the J_{sc} of the BP-SC is 1.6 times the J_{sc} of the Flat-SC device for 650 nm light, and 3.4 times for 750 nm light.

The broadband light-trapping achieved with the TiO_2-NP/Si-NP bilayer with inverted pyramid features in the present study brings out the benefits of BLiS back-reflectors based on nanoparticles having different refractive indices. The low-cost, simplified nanofabrication method presented is scalable, circumvents the complicated approaches of mechanical and chemical flattening of light trapping microstructures and opens up the path to optical management that is less constrained by the shape or roughness of the nanostructures. In addition, the excellent electrical performance of the solar cells on the BLiS back-reflectors for a wide distribution of angles of incidence also shows the potential for a better and consistent diurnal performance of the solar cells.

4 Conclusion

Micro-sized inverted-pyramid-shaped microcavities were made in a layer of TiO_2-NPs, over a planar reflector to create a light-management layer for thin-film solar cells. In another design, a flat-topped Si-NP layer was molded over the inverted pyramid TiO_2-NP layer to create Si-NP inverted pyramids in the cores of the TiO_2 microcavities. The Si-NP/TiO_2-NP bilayer back reflector has buried textures and a smooth surface for the subsequent growth of solar-cell layers. The investigations show an increased light-scattering and improvement in solar cell performance over a broad wavelength range as well as over a range of incident angles. Both designs lead to increased light-scattering, but the exposed inverted pyramid TiO_2 layer leads to a decrease in the solar cell efficiency and fill factor due to the detrimental effect of a rough solar cell growth interface. The gains in the efficiency and the short-circuit current density are up to 17.5% and 14%, respectively, in the a-Si:H thin-film solar cell grown on the buried inverted pyramid bilayer back-reflector. The industry-friendly technique of fabrication of BLiS textures is inexpensive, scalable and straightforward. Our study brings out the benefit of using optically dissimilar nanoparticles for creating buried nano- and micro-scale light manipulating textures for devices where it is desirable to avoid morphological roughness.

Supplementary Material

The Supplementary Material contains the details of the FDTD simulation model, the cross-sectional FIB-SEM images of the BLiS solar cell device, the surface topography images of the back-reflectors and the calculated optical absorption of the flat and BLiS solar cell devices.

The Supplementary Material is available at https://www.epj-pv.org/10.1051/epjpv/2019011/olm.

The authors acknowledge support from the Danish Strategic Research Council under the project 'THINC' and from the Innovation Fund Denmark under the project 'SunTune'. We thank Hartmut Wiggers for providing Si-NPs for this work, Yao-Chung Tsao for the angular reflectivity measurements of the back-reflectors, and Pia B. Jensen for FIB-SEM measurements. D.D. and R.N.P. also acknowledge the financial support by the

project I3N (UID/CTM/50025/2019), financed by national funds through the Fundação para a Ciência e a Tecnologia/Ministério da Educação e Ciência (FCT/MEC) and co-financed by FEDER under the PT2020 Partnership Agreement, as well as the financial support of FCT (Fundação para a Ciência e a Tecnologia) via projects PTDC/FIS/112885/2009, PTDC/CTM-ENE/2514/2012, and RECI/FIS-NAN/0183/2012 (FCOMP-01-0124-FEDER-027494).

Author contribution statement

S.K.R. conceived the methodology used for the nanomolded buried light-scattering back-reflectors (BLiS) and coordinated the overall research work; D.D. performed the basic fabrication and characterization of BLiS structures and FDTD calculations; R.R. and C.S. led the silicon layer development work; S.K.R. and R.R. performed the characterization and the data analyses; A.N.L., R.N.P. and P.B. contributed to data interpretation; D.D. and S.K.R. wrote the manuscript with relevant contributions from all the authors.

References

1. J. Nelson, *Physics of Solar Cell* (Imperial College Press, London, 2008)
2. A.V. Shah, H. Schade, M. Vanecek, J. Meier, E. Vallat-Sauvain, N. Wyrsch, U. Kroll, C. Droz, J. Bailat, Prog. Photovolt: Res. Appl. **12**, 113 (2004)
3. V.E. Ferry, M.A. Verschuuren, H.B.T. Li, E. Verhagen, R.J. Walters, R.E.I. Schropp, H.A. Atwater, A. Polman, Opt. Express **18**, A237 (2010)
4. F.J. Haug, C. Ballif, Energy Environ. Sci. **8**, 824 (2015)
5. H.W. Deckman, C.R. Wronski, H. Witzke, E. Yablonovitch, Appl. Phys. Lett. **42**, 968 (1983)
6. H.-P. Wang, D.-H. Lien, M.-L. Tsai, C.-A. Lin, H.-C. Chang, K.-Y. Lai, Jr. H. He, J. Mater. Chem. C **2**, 3144 (2014)
7. M.L. Brongersma, Y. Cui, S. Fan, Nature Mater. **13**, 451 (2014)
8. C.F. Guo, T. Sun, F. Cao, Q. Liu, Z. Ren, Light: Sci. Appl. **3**, e161 (2014)
9. M.A. Green, *Si Solar Cells: Advanced principles and practice* (Bridge Printery, Sydney, 1995)
10. K.X. Wang, Z. Yu, V. Liu, Y. Cui, S. Fan, Nano Lett. **12**, 1616 (2012)
11. H.-H. Cheng, Y.-Y. Chang, J.-Y. Chu, D.-Z. Lin, Y.-P. Chen, J.-H. Li, Appl. Phys. Lett. **101**, 141113 (2012)
12. J. Escarré, K. Söderström, M. Despeisse, S. Nicolay, C. Battaglia, G. Bugnon, L. Ding, F. Meillaud, F.-J. Haug, C. Ballif, Sol. Energy Mater. Sol. Cells **98**, 185 (2012)
13. G. Li, H. Li, J. Ho, M. Wong, H.S. Kwok, in *29th European Photovoltaic Solar Energy Conference and Exhibition, Amsterdam, The Netherlands, 2014*
14. S.C. Baker-Finch, K.R. McIntosh, Prog. Photovolt: Res. Appl. **19**, 406 (2011)
15. S.E. Han, G. Chen, Nano Lett. **10**, 4692 (2010)
16. G. Li, H. Li, J.Y. Ho, M. Wong, H.S. Kwok, Nano Lett. **14**, 2563 (2014)
17. L. Hu, G. Chen, Nano Lett. **7**, 3249 (2007)
18. J. Zhao, A. Wang, M.A. Green, F. Ferrazza, Appl. Phys. Lett. **73**, 1991 (1998)
19. M.M. de Jong, P.J. Sonneveld, J. Baggerman, C.J.M. van Rijn, J.K. Rath, R.E.I. Schropp, Prog. Photovolt: Res. Appl. **22**, 540 (2014)
20. H.B.T. Li, R.H. Franken, J.K. Rath, R.E.I. Schropp, Sol. Energy Mater. Sol. Cells **93**, 338 (2009)
21. T. Soderstrom, F.J. Haug, V. Terrazzoni-Daudrix, C. Ballif, J. Appl. Phys. **103**, 114509 (2008)
22. C.-M. Hsu, C. Battaglia, C. Pahud, Z. Ruan, F.-J. Haug, S. Fan, C. Ballif, Y. Cui, Adv. Energy Mater. **2**, 628 (2012)
23. D. Desta, S.K. Ram, R. Rizzoli, M. Bellettato, C. Summonte, B.R. Jeppesen, P.B. Jensen, Y.-C. Tsao, H. Wiggers, R.N. Pereira, P. Balling, A.N. Larsen, Nanoscale **8**, 12035 (2016)
24. Y. Nasuno, M. Kondo, A. Matsuda, Jpn. J. Appl. Phys. **2**, L303 (2001)
25. D. Wang, G. Su, Sci. Rep. **4**, 7165 (2014)
26. A.P. Vasudev, J.A. Schuller, M.L. Brongersma, Opt. Express **20**, A385 (2012)
27. K.J. Byeon, H. Lee, Eur. Phys. J. Appl. Phys. **59**, 10001 (2012)
28. Y.A. Akimov, W.S. Koh, S.Y. Sian, S. Ren, Appl. Phys. Lett. **96**, 073111 (2010)
29. C. Hsu, G.F. Burkhard, M.D. McGehee, Y. Cui, Nano Res. **4**, 153 (2011)
30. S.K. Ram, R. Rizzoli, D. Desta, B.R. Jeppesen, M. Bellettato, I. Samatov, Y.-C. Tsao, S.R. Johannsen, P.T. Neuvonen, T.G. Pedersen, R.N. Pereira, K. Pedersen, P. Balling, A.N. Larsen, J. Phys. D: Appl. Phys. **48**, 365101 (2015)
31. H. Sai, Y. Kanamori, M. Kondo, Appl. Phys. Lett. **98**, 113502 (2011)
32. K. Soderstrom, G. Bugnon, F.J. Haug, S. Nicolay, C. Ballif, Sol. Energy Mater. Sol. Cells **101**, 193 (2012)
33. R.N. Pereira, S. Niesar, W.B. You, A.F. da Cunha, N. Erhard, A.R. Stegner, H. Wiggers, M.G. Willinger, M. Stutzmann, M.S. Brandt, J. Phys. Chem. C **115**, 20120 (2011)
34. A. Gupta, M.T. Swihart, H. Wiggers, Adv. Funct. Mater. **19**, 696 (2009)
35. E.D. Palik, ed., *Handbook of optical constants of solids* (Academic Press, 1998)
36. M.W.M. van Cleef, F.A. Rubinelli, R. Rizzoli, R. Pinghini, R.E.I. Schropp, W.F. van der Weg, Jpn. J. Appl. Phys. **37**, 3926 (1998)
37. C. Battaglia, S.M. de Nicolas, S. De Wolf, X.T. Yin, M. Zheng, C. Ballif, A. Javey, Appl. Phys. Lett. **104**, 113902 (2014)
38. J.K. Rath, R.E.I. Schropp, Sol. Energy Mater. Sol. Cells **53**, 189 (1998)
39. Y. Zhang, H. Liu, Crystals **9**, 87 (2019)
40. R.H. Franken, R.L. Stolk, H. Li, C.H.M. van der Werf, J.K. Rath, R.E.I. Schropp, J. Appl. Phys. **102**, 014503 (2007)
41. P. Kowalczewski, M. Liscidini, L.C. Andreani, Opt. Express **21**, A808 (2013)

Cite this article as: Derese Desta, Rita Rizzoli, Caterina Summonte, Rui N. Pereira, Arne Nylandsted Larsen, Peter Balling, Sanjay K. Ram, Nanomolded buried light-scattering (BLiS) back-reflectors using dielectric nanoparticles for light harvesting in thin-film silicon solar cells, EPJ Photovoltaics **11**, 2 (2020)